small methods
www.small-methods.com

Gradient Doping Strategy for Sn—Pb Mixed Perovskite Solar Cells with High Efficiency and Stability

Haotian Zhang, Chao Gao, Li He, Dezhao Zhang, Hongzhen Su, Hong Liu, Kadi Zhu, and Wenzhong Shen**

Sn—Pb hybrid perovskite has attracted more attention due to its ideal bandgap and excellent photoelectric properties. However, easy oxidation and poor crystallinity caused by the introduction of Sn^{2+} have become two major problems. In this study, Sn^{2+} is doped in the Pb-based perovskite to prepare high crystalline Sn—Pb mixed perovskite with larger grain size by using the solvent engineering technique and the cooperation optimization with HCOOH. The reducibility of HCOOH and its inhibition of deprotonation significantly prevent the oxidation of Sn^{2+} and the decomposition of A-site cations. The experimental and theoretical results show that the interactions between HCOOH and Sn^{2+} and Pb^{2+}, which reduce the defect density and improve the crystallinity and stability of the film with excellent photoelectric properties. In addition, the compact SnO_2 prepared by atomic layer deposition as electronic transformation layer to further improve the stability of devices. The photoelectric conversion efficiency of the Sn—Pb hybrid perovskite solar cells (PSCs) prepared by the dopant growth method can reach 21.53% and the stability is significantly better than that of the Sn—Pb PSCs prepared by the traditional method.

1. Introduction

Organic–inorganic halide perovskite solar cells (PSCs) have developed rapidly in the past few decades and have attracted extensive attention due to their excellent photoelectric properties such as high absorption coefficient and carrier diffusion length.[1–8] The power conversion efficiency (*PCE*) has also increased from initial 3.8% to the current record of 27.0%.[9–11] However, its potential for commercialization is limited due to its stability and toxicity.[12–14] The stability challenges of Pb-based perovskite are being addressed by virtue of 2D perovskites and improved encapsulation technologies.[15,16] Toxicity can be solved by non-Pb containing materials instead of traditional Pb-based perovskite materials, such as Ge, Sb, Bi, and Sn and other materials are considered to be promising to replace Pb as new generation of environmentally friendly and non-toxic PSCs materials.[12,17–20] Among these materials, Sn is regarded as the most promising material to replace Pb in perovskite because of their similar ionic radius and electron configuration.[21,22] Sn—Pb hybrid perovskite has highly anticipated as a good compromise due to its latent capacity for both high *PCE* and stability. The addition of Sn will contribute to regulate suitable bandgap to achieve 33.7% *PCE* limit predicted by Shockley–Queisser (S—Q) theory.[23–25] Sn—Pb mixed perovskite can be widely applied to tandem devices since the adjustability of its bandgap.[26–28] However, easy oxidation of Sn^{2+} to $Sn^{4+}$and the uncontrollability of Sn—Pb perovskite film crystallization leads to vacancy defects during film formation, which constraints the *PCE* and stability further improvement of Sn—Pb PSCs.[22,29–32]

In order to solve Sn^{2+} oxidation and poor crystallinity in Sn—Pb mixed perovskite, series of studies have been conducted.[33,34] Excessive Sn powder or SnF_2 are introduced into the precursor solution as Sn compensator to provide Sn-rich environmental compensation and prevent the oxidation of Sn^{2+}.[35,36] Density functional theory calculations have demonstrated that the defect density of the film can be reduced because the formation energy of Sn vacancy (V_{Sn}) will be increased in a Sn-rich environment.[37,38] The Sn^{2+} loss caused by oxidation or intrinsic V_{Sn} formation can be compensated by a compensator. Studies also have shown that Sn^{2+} is thermodynamically stable in acidic medium.[39] Acetic Acid can be applied to provide a weak acid environment and passivate undesired Sn defects in perovskite films.[40] Additionally, the employment of SnC_2O_4, phenylhydrazine thiocyanate and other antioxidants are also

H. Zhang, C. Gao, L. He, D. Zhang, H. Su, H. Liu, W. Shen
Institute of Solar Energy
and Key Laboratory of Artificial Structures and
Quantum Control (Ministry of Education)
School of Physics and Astronomy
Shanghai Jiao Tong University
Shanghai 200240, P. R. China
E-mail: wzshen@sjtu.edu.cn

H. Zhang, C. Gao, L. He, D. Zhang, H. Su, H. Liu, W. Shen
Shanghai Non-carbon Energy Conversion and Utilization Institute
Shanghai 200240, P. R. China

K. Zhu
School of Physics and Astronomy
Shanghai Jiao Tong University
Shanghai 200240, P. R. China
E-mail: zhukadi@sjtu.edu.cn

W. Shen
Collaborative Innovation Center of Advanced Microstructures
Nanjing 210093, P. R. China

The ORCID identification number(s) for the author(s) of this article can be found under https://doi.org/10.1002/smtd.202500064

DOI: 10.1002/smtd.202500064

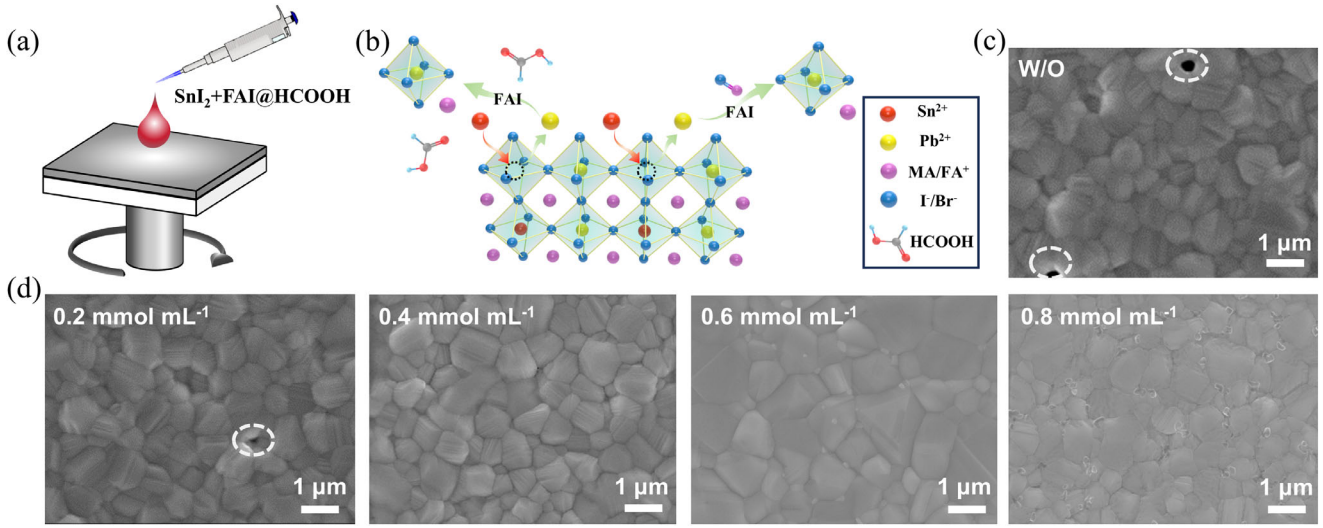

Figure 1. a) The operating procedure for the synthesis of Sn—Pb mixed perovskite film. b) Schematic diagram of Sn^{2+}-doped perovskite film process. c) Top-view SEM images of Pb-based perovskite film and d) Sn—Pb mixed perovskite film at different SnI_2+FAI@HCOOCs concentrations.

effective ways to alleviate Sn^{2+} oxidation.[41–43] Although the defects and the oxidation of Sn^{2+} can be prevented by reductive ions through solvent engineering, the stability improvement is not satisfactory and the grain size are still significantly smaller than Pb-based perovskite, which will negatively affect the photoelectric properties of the films. Therefore, new growth method of Sn—Pb mixed perovskite with high stability and high *PCE* is an important problem to be investigated. HCOOH has been proven to effectively inhibit the deprotonation of perovskites and improve the crystallinity of perovskites.[44,45] Our group reported the growth of highly stable wide-band gap Cs-based perovskites by in situ substitution of A-site ions on Pb-based perovskites using HCOOCs@HCOOH without damaging morphology of underlying film.[46] Meanwhile, formic acid also has reducing properties and weak acidity, which contribute to the stability of Sn^{2+} as mentioned before.[40] These studies provide conditions for development of our new growth method to prepare Sn—Pb mixed perovskite with high crystallization and stability by doping Sn in place of Pb.

Herein, we report the synthesis of Sn—Pb mixed perovskite films by in situ gradient doping on Pb-based perovskite with SnI_2+FAI@HCOOH solution. Under the synergistic optimization of formic acid, Pb^{2+} has been partial replaced by Sn^{2+}, and Sn—Pb mixed perovskite has been obtained. The excess PbI_2 reacts with FAI to form perovskite and passivate the defect, which can be proved by series of characterizations. It is worth mentioning that because it is doped with the underlying perovskite as the frame, it retains the integrity of the original Pb-based perovskite grains and the grains are much higher than those of the Sn—Pb mixed perovskite films prepared by traditional solution method, which exhibit better crystallinity and excellent photoelectric properties. The vacancy defects in perovskite are reduced and the oxidation of Sn^{2+} is significantly inhibited due to the reducibility of HCOOH and the inhibition of deprotonation reaction, which greatly enhances the stability of the devices. The suitable energy level alignment of doped films can effectively suppress the nonradiative recombination of carriers and improve the charge transfer in the devices. The dense SnO_2 prepared by atomic layer deposition (ALD) with PCBM as double layer ETL can further improve the stability of the devices. Eventually, the champion device has a *PCE* of 21.53%, and the stability remains 85% of the initial efficiency after 3000 h. In addition, it also has outstanding performance in terms of thermal stability and illumination stability.

2. Result and Discussion

Pb-based perovskite film was prepared by one-step spin-coating method via an anti-solvent method as underlying film. Then SnI_2 and FAI dissolved in formic acid spin coat on the Pb-based perovskite film as shown in **Figure 1**a. Figure 1b shows that Sn^{2+} will penetrate the underlying layer (MAFA)Pb(I, Br)$_3$ with the help of formic acid following partially replaces Pb^{2+} to form Sn—Pb mixed perovskite films (MAFA)(Pb, Sn)(I, Br)$_3$. To confirm that the substitution process takes place, a series of experiments are applied to the different samples. First, we apply SnI_2+FAI@HCOOH on ITO to confirm whether it generates perovskite film on the underlying film. Figure S1 (Supporting Information) displays the X-ray diffraction (XRD) results after being spin-coated with SnI_2+FAI@HCOOH on ITO substrate. The pattern of the film is the same as ITO, where the difference of peak intensity is attributed to the difference between ITO substrate. The result indicates that SnI_2+FAI@HCOOH cannot generate $FASnI_3$ crystalline phase film on the underlying Pb-based perovskite. Then SnI_2 solution dissolved in formic acid is employed directly on the Pb-based perovskite film and an extra peak appears in Figure S2 (Supporting Information). According the XRD pattern of PbI_2 and SnI_2 powder in Figure S3 (Supporting Information), the extra peak turns out to be PbI_2 and no SnI_2 peak observed in Figure S2 (Supporting Information). Moreover, Figure S2 (Supporting Information) shows the XRD peak intensity of PbI_2 will gradually enhance with the increasing of SnI_2 solution concentration. Experiments are conducted to explore the formation mechanism of PbI_2. Figure S4 (Supporting Information) shows the XRD pattern after HCOOH spin-coated

on perovskite with no extra peaks. Therefore, the appearance of PbI_2 in Figure S2 (Supporting Information) is affected by SnI_2 rather than HCOOH. It is reasonable to deduce that the introduction of Sn^{2+} displaces Pb^{2+} in perovskite film and produces additional lead iodide. The (100) peak of perovskite shifts to the higher degree gradually with the larger concentration, which is consistent with the case of Sn^{2+} with smaller radius replacing Pb^{2+}.[21,47] This result indicates that Sn^{2+} replaces Pb^{2+} in the perovskite lattice. Top-view scanning electron microscope (SEM) images in Figure S5 (Supporting Information) show that the morphology changes of PbI_2 with the increasing concentration solution, which are consistent with XRD results. Adding moderate FAI to SnI_2@HCOOH can appropriately generate $FAPbI_3$ to reduce excess PbI_2, which effectively avoids degeneration of the film.[48] As shown in Figure 1c, the SEM image of the underlying Pb-based perovskite film exhibit excellent crystallinity, however there are still a few pinholes. The SEM morphology of the underlying films treated with SnI_2+FAI@HCOOH solution of different concentrations shows that PbI_2 can be reacted by FAI when the proportion of SnI_2+FAI@HCOOH solution is appropriate (Figure 1d). The generated $FAPbI_3$ can effectively fill the defect pinholes in the underlying perovskite film, which can improve the quality of the film. When the concentration is lower, the defects cannot be filled enough to obtain uniform morphology and the Sn content is not sufficient. While the concentration is too high, excessive PbI_2 will be generated without reacting with FAI in time. The optimal doping concentration is 0.4 mmol mL^{-1}. Table S1 (Supporting Information) shows that the device champion efficiency fabricated by different types of acids tried during the doping processes under all fabrication conditions. The details of the fabrication process for device are also demonstrated in Supporting Information. It is demonstrated that the devices using formic acid for doping process exhibits excellent performance. In addition, doping time is also an important parameter that affects the performance of the corresponding thin film devices in Table S1 (Supporting Information). It is understandable that short doping time cannot ensure fully doping of Sn^{2+} affecting the device performance, but the negative effect of long doping time on the film still needs further investigation. To further understand Sn—Pb mixed perovskite in longer doping time condition, high resolution grazing incidence X-ray diffraction (GIXRD) measurement was conducted on the samples with 0.4 mmol mL^{-1} doping solution concentration and different doping time. Figure S6 (Supporting Information) shows the significant shift of the (100) peak of Sn—Pb mixed perovskite film relative to Pb-based film, which is consistent with the previous XRD result. It is worth noting that the phase separation Sn—Pb mixed film is found in 7s doping time condition, which have two peaks in GIXRD pattern representing Pb-based and Sn-based perovskite respectively. The interface and defect generated by phase separation could become the recombination centers that reduce the effective carriers collected by the electrode, reducing the device performance. Although Sn—Pb mixed perovskite without phase separation is needed, the phenomenon illustrates the formation of Sn-based perovskite. In addition, the result shows that there is no PbI_2 peaks, which is further proved that PbI_2 and FAI reacted adequately. Moreover, GIXRD test at different incident angles were also applied to the 0.4 mmol mL^{-1} doping sample in Figure S7 (Supporting Information), the results showed that the peak position of the sample was larger at smaller angle of incidence, which indicated that the Sn gradient distribution of the Sn—Pb mixed perovskite.

To further confirm the distribution of Sn in Sn—Pb mixed perovskite, time-of-flight secondary ion mass spectroscopy (TOF-SIMS) was performed on samples with 0.4 mmol mL^{-1} doping solution concentration. **Figure 2a–c** show the vertical elements gradient distribution of the underlying film and doping film. Argon Gas Cluster Ion Beam (Ar-GCIB) was used for sputtering process to prevent introducing ions that interfere with the result. The distribution concentration of Sn^{2+} after modification is greatly increased and accompanied by certain $HCOO^-$ penetration. The distribution of Sn^{2+} on the surface exhibit obvious changes and the concentration of Sn—Pb mixed perovskite decreases gradually with the enhancement of depth then the Sn^{2+} concentration tends to be uniform when it is still dozens of times that of the Pb-based film. The vertical distribution of other elements is shown in Figure S8 (Supporting Information), which illustrates that there is no other significant difference between two samples. The element distribution of modified perovskite film surface is also investigated by energy dispersive spectroscopy (EDS) mapping in Figure 2d. The results show enrichment of Sn and relatively uniform mixture of Sn—Pb on the sample. Figure S9 (Supporting Information) displays the distribution of other elements in the modified sample. In addition, the characterization of Sn characteristic peaks by X-ray photoelectron spectroscopy (XPS) in also proves the success of Sn doping (Figure 2e).

To further characterize the crystalline of the film, XRD test is conducted in the different conditions of preparation of Sn—Pb mixed perovskite (0.2, 0.4, and 0.6 mmol mL^{-1}). Figure 2f shows that the (100) peaking intensity with appropriate concentration (0.4 mmol mL^{-1}) exhibit narrower FWHM than the original film, indicating that Sn^{2+} almost replaces Pb^{2+} in the lattice without any lattice distortion. The generated $FAPbI_3$ effectively filled the pinholes in the film. The presence of $HCOO^-$ effectively inhibits the anion vacancy defects at the grain boundary and surface of perovskite films, thus increasing the crystallinity of the films.[44] Combined with the TOF-SIMS test, Sn^{2+} distributes uniformly on the surface of the doping sample with a concentration of 0.4 mmol mL^{-1}. As the increase of doping concentration, the generated PbI_2 cannot be completely reacted into perovskite by FAI and the characteristic peak of PbI_2 appears in the XRD pattern, which is consistent with the results of SEM measurement. In addition, the peak of (100) shows a significant shift to large degree when the doping concentration increases, which is attributed to the smaller radius of Sn^{2+}, resulting in lattice shrinkage and increase in diffraction angle (Figure 2g). The similar phenomenon can be detected in the earlier GIXRD results. The formation of orthorhombic yellow phase (δ-phase) cannot be found during the replacement process. The δ-phase in perovskite as the trapping and scattering center would significantly reduce the photoelectric performance of the device and carrier mobility in semiconductor films.[45] This can be attributed to the inhibiting effect of HCOOH on oxidation of iodide ions and deprotonation of A-site atoms in perovskite.[44]

Subsequently, the optical properties of the doping films were characterized and analyzed to further explore the changes of doping material. The UV–vis absorption spectra of doping film in Figure 2h shows significant red shift of absorption edges

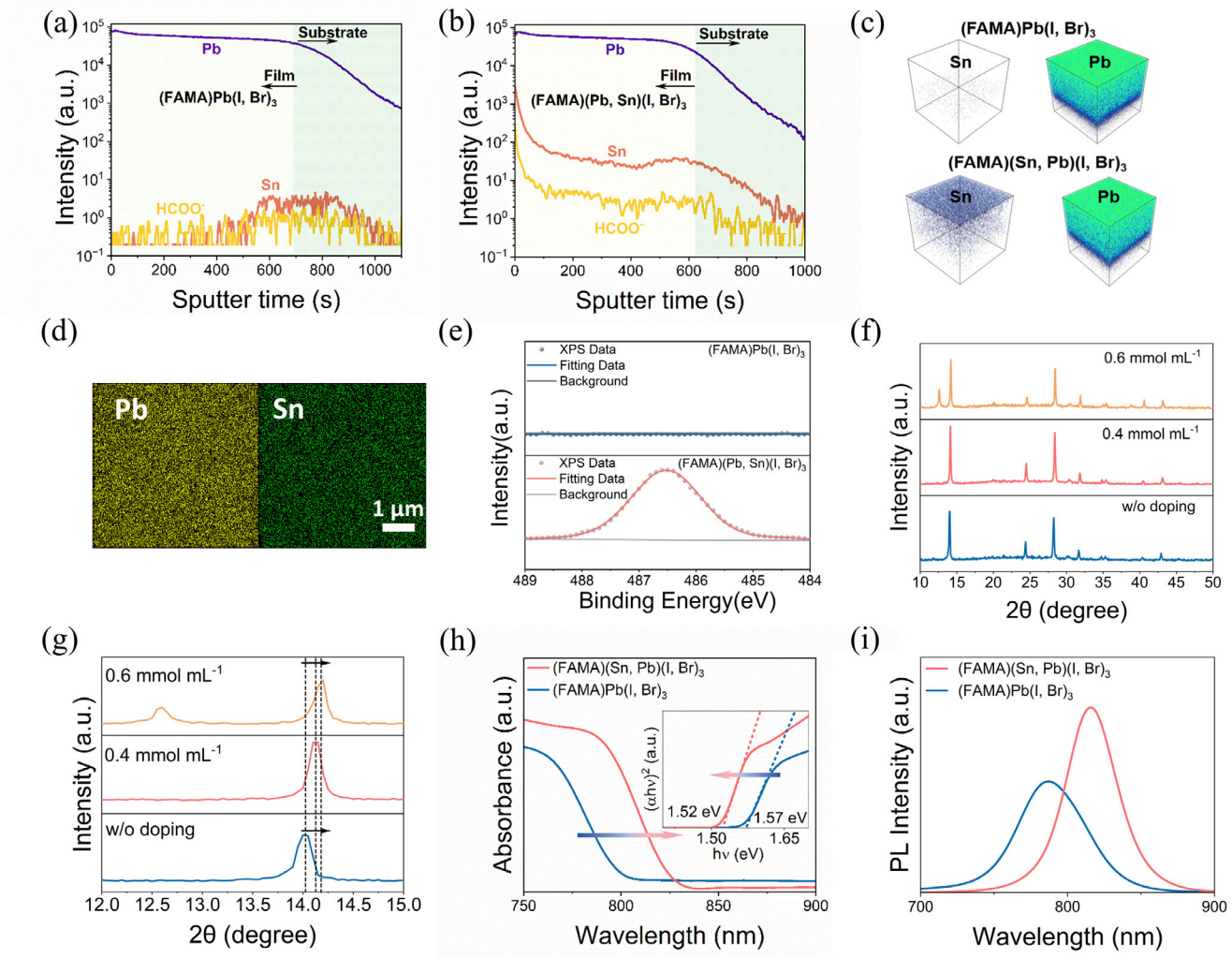

Figure 2. TOF-SIMS depth profiles of a) underlying Pb-based perovskite film and b) doping Sn—Pb perovskite film. c) 3D distribution of Sn/Pb elements for underlying Pb-based perovskite film (up) and doping Sn—Pb perovskite film (down). d) EDS mapping of Sn, Pb elements of Sn—Pb perovskite film. e) XPS spectral of samples for the position of Sn characteristic peak. f) XRD pattern of perovskite film. g) (100) peak of perovskite film in XRD pattern. h) UV–vis absorption spectra of the corresponding samples. i) PL spectra of different films.

relative to the underlying perovskite. The band gap of the underlying film and the doping film is 1.57 and 1.52 eV, respectively, which is due to the narrow band gap characteristics of Sn—Pb mixed perovskite. The light absorption of the doping film exhibits higher light utilization efficiency in the wider wavelength range spectrum (600–900 nm) due to the passivation modification of $HCOO^-$ (Figure S10, Supporting Information), which is consistent with crystallinity enhancement in the previous XRD results. The steady-state photoluminescence (PL) spectra are shown in Figure 2i, the peak shifted from 786 to 816 nm with the increase of peak strength also indicates the synergistic effect of doping process and modification passivation. In addition, PL mapping images in Figure S11 (Supporting Information) shows that the doping sample has a luminescence intensity many times stronger than before at the wavelength between 800 and 830 nm. The transfer of luminescence wavelength range indicates that the doping film has changed from Pb-based perovskite (wide-bandgap) to Sn—Pb mixed perovskite (narrow-bandgap). Figure S12 (Supporting Information) shows the time-resolved PL (TRPL) results for half-devices with underlying and doping perovskite. The doping perovskite film exhibits faster TRPL decay, implying a stronger carrier extraction capability. To verify the origin of the better carrier extraction ability, ultraviolet photoelectron spectroscopy (UPS) is performed on the samples. As shown in Figure S13 (Supporting Information), the maximum valence band value (VBM) and minimum conduction band value (CBM) of the sample can be calculated with the optical band gap obtained by the UV–vis absorption spectrum, and the energy level arrangement diagram in the device can be obtained in Figure S14 (Supporting Information). The Fermi level and CBM are effectively increased due to doping process and $HCOO^-$ modification on the crystallinity of the films, which is more conducive to carrier transport. The result explains the faster TRPL decay in doping films. In conclusion, all above characterizations of the underlying film and doping film elucidate that Sn—Pb mixed perovskite films with good crystalline and optical properties are prepared

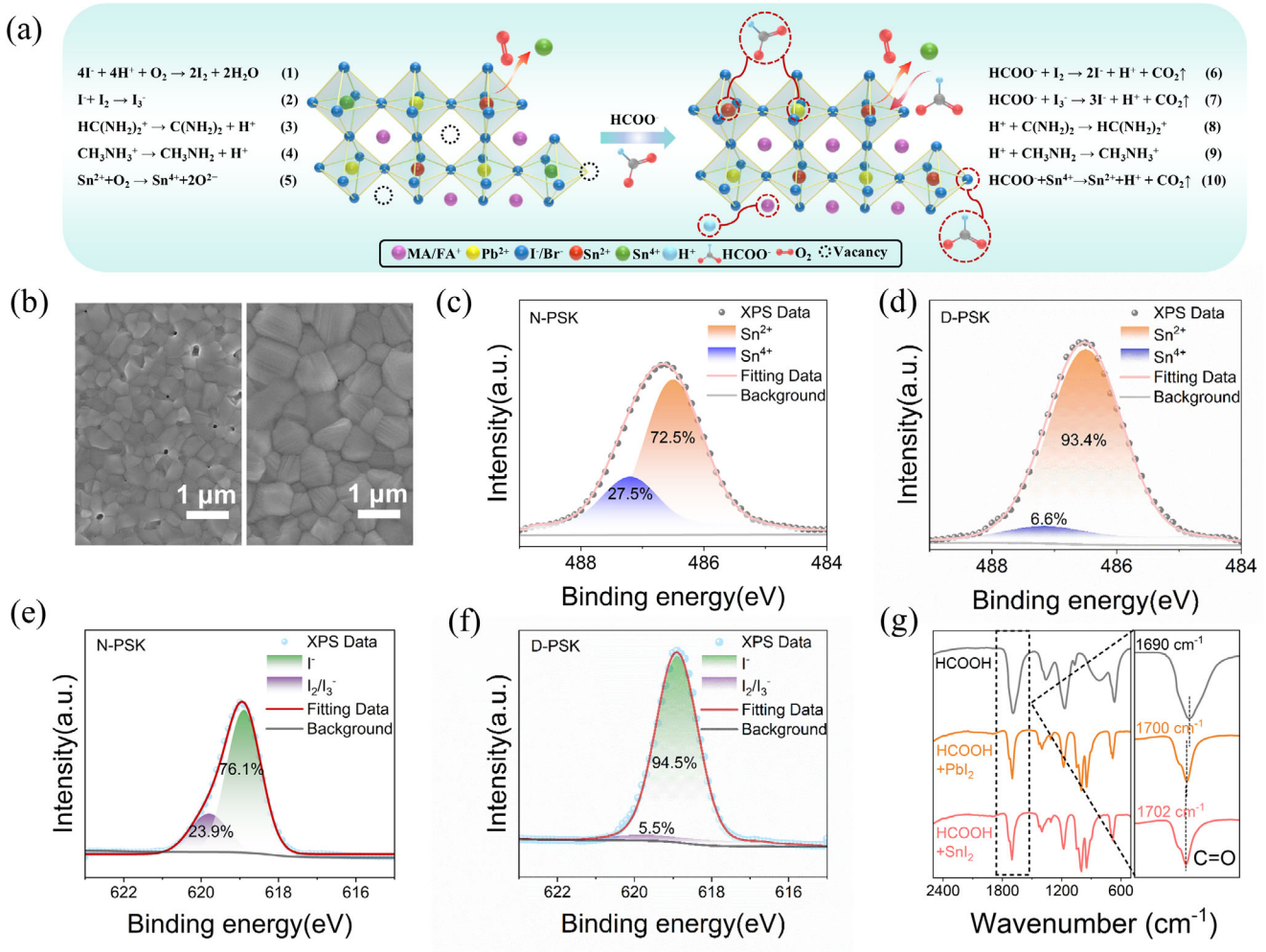

Figure 3. a) Schematic illustration for the function of $HCOO^-$ in perovskite films and reaction process. b) Top-view SEM images of normal Sn—Pb and doping Sn—Pb perovskite film. XPS spectra for Sn 3d c,d) and I 3d e,f) of normal Sn—Pb and doping Sn—Pb perovskite films. g) FTIR spectra of pure HCOOH, HCOOH +SnI_2 complex, and HCOOH +PbI_2 complex in DMSO.

by HCOOH combination using Pb-based perovskite with good crystalline properties as the framework.

Compared with the common Sn—Pb mixed perovskite film prepared by solutions method, the doping Sn—Pb mixed perovskite film (doping perovskite, D-PSK) exhibits better performance. Different components films are prepared by spinning-coat Sn—Pb precursor solutions of different concentrations.[49] The PL spectra tests on samples of different Sn—Pb proportions, as shown in Figure S15 (Supporting Information), the $(FAPbI_3)_{0.855}(MAPbBr_3)_{0.095}(FASnI_3)_{0.05}$ perovskite film (normal perovskite, N-PSK) is utilized as control sample to compare with the D-PSK film because of the similar bandgap, demonstrating the advantages of D-PSK films. The function of $HCOO^-$ in the perovskite film is illustrated in **Figure 3a** and each process corresponds to the chemical formula on the side. In N-PSK, I^- is oxidized to I_2 by oxygen of the air dissolved in the precursor solution and I^- is further combined with I_2 to form I_3^- (Equations 1 and 2). FA^+ and MA^+ will be decomposed due to the deprotonation reaction in (Equations 3 and 4). Oxidation and deprotonation reactions will cause the imbalance of the proportion of atoms in the lattice and promote the formation of δ phase. The oxidation of Sn^{2+} (Equation 5) will make a negative impact on device performance. In the D-PSK sample, the reduction of HCOOH can effectively prevent the oxidation of I^- and Sn^{2+} (Equation 6, 7, 10). While the weak acid environment provided by HCOOH can significantly inhibit the deprotonation reaction of FA^+ and MA^+ (Equations 8 and 9), which greatly improves the stability of D-PSK. In addition, large pinholes exist on N-PSK films due to the uncontrollable crystallization in the film preparation process and the crystal grains are much smaller than those of traditional Pb-based perovskite. In contrast, D-PSK is permeated and doped on the well-grown Pb-based perovskite framework (Figure 3b). Therefore, the grain size can be retained in the original size. Larger grain size and better crystallinity are conducive to carrier transport and effectively inhibits the occurrence of non-radiative recombination. XRD measurement in Figure S16 (Supporting Information) of N-PSK and D-PSK samples shows that the D-PSK sample shows decreased FWHM values and stronger diffraction intensity compared with the N-PSK sample. This means better crystallinity of the D-PSK

sample, which is related to $HCOO^-$ modification and fewer defect in the sample. To further investigate the reductive effect of $HCOO^-$ on Sn^{4+} and I_2/I_3^-, XPS measurements were conducted to analyze the characteristic peaks of Sn and I in N-PSK and D-PSK samples. XPS peak of Sn $3d_{5/2}$ could be divided into two sub-peaks as shown in Figure 3c,d, corresponding to Sn^{4+} higher energy peak (487.2 eV) and Sn^{2+} lower energy peak (486.5 eV), respectively.[40] According to the peak fitting results, the contents of Sn^{4+} and Sn^{2+} in N-PSK sample are ≈27.5% and 72.5%, while the contents of Sn^{4+} and Sn^{2+} in D-PSK sample are 6.6% and 93.4%, respectively. The oxidized content of Sn^{2+} is significantly reduced. As shown in Figure 3e,f, it can be seen that the content of I_2/I_3^- also decreases from 23.9% in N-PSK samples to 5.5% in D-PSK samples, indicating that $HCOO^-$ prevents the oxidation process of iodide ions.[40] Furthermore, the XPS measurements were used to test the ratio of I/Br of N/D-PSK samples to ensure the reductive effect of HCOOH in Figure S17 (Supporting Information). According the result, the ratio of I/Br in D-PSK was determined to be 9.17 ± 0.36 and 7.25 ± 0.54 in N-PSK by XPS measurements. The substantial iodide deficiency indicates that I^- ions were oxidized during the crystallization process without HCOOH in N-PSK film, which illustrate the reductive effect of HCOOH plays important role during the crystallization process. Meanwhile, Fourier transform infrared spectroscopy (FTIR) is used to study the interaction between $HCOO^-$ and Pb^{2+} and Sn^{2+} in perovskite (Figure 3g). In contrast to FTIR spectrum of the PbI_2/SnI_2 dissolved in DMSO (Figure S18, Supporting Information), the emerging peak at 1700 and 1702 cm^{-1} can be attributed to O═C─O, indicating that $HCOO^-$ is successfully doped into the perovskite. The peaks corresponding to $HCOO^-$ (O═C─O) are shifted in the mixed solution of HCOOH and PbI_2/SnI_2, indicating the interaction between C═O and Sn^{2+}/Pb^{2+}. As a Lewis base, C═O of HCOO- can form coordination bonds with unpaired Sn^{2+}/Pb^{2+} and passivate defects through Lewis acid-base interaction, improving the performance and stability of the devices.[49] Besides, the shift of the O═C─O deformation peak toward a higher wave number means an interaction between $HCOO^-$ and perovskite. However, Sn^{2+} and Pb^{2+} exist simultaneously in Sn—Pb mixed perovskite. It is necessary to ensure that HCOOH can interact with both of them at the same time to passivate perovskite, instead of losing its passivating effect on the other atom due to stronger interaction with Sn^{2+} or Pb^{2+}. The independent gradient model based on Hirshfeld partition (IGMH) was used to visualize the interactions in the system (Figure S19, Supporting Information). The result shows that the interaction strength between HCOOH and Pb^{2+} is similar to Sn^{2+}. The more elaborate interaction energy results based on density functional theory (DFT) show that the interaction energy of HCOOH with Pb^{2+} is −0.836 eV, while the interaction energy of HCOOH with Sn^{2+} is −0.844 eV. This indicates that in the Sn—Pb mixed perovskite, both Sn^{2+} and Pb^{2+} can interact with HCOOH to passivate perovskite, and Sn^{2+} is slightly preferentially passivated. The details of calculations are provided in theoretical section of SI. The D-PSK samples modified by HCOOH exhibit better crystallinity and stability than N-PSK samples due to the reducibility of HCOOH and its interaction with perovskite atoms.

The optical and electrical properties are also significant criteria of the photoelectric materials. The UV–vis spectral in **Figure** 4a illustrates that D-PSK film has stronger light absorption than N-PSK film. The stronger intensity is detected by PL spectra in Figure 4b and PL mapping spectral in Figure 4d,e also illustrate that the overall luminous intensity of D-PSK sample is obviously stronger than N-PSK, which is attributed to the D-PSK has better crystallinity and fewer defects. Figure 4c and Figure S20 (Supporting Information) exhibit TRPL measurement result of D/N-PSK half devices. The average carrier lifetime (τ_{avg}) of the N/D-PSK device can be obtained through the double exponential fitting of the data (Table S2, Supporting Information). The faster TRPL decay indicates the strong carrier separation ability at the sample interface and the better crystallinity of perovskite. The reason for this superior carrier dynamic behavior is further confirmed by UPS. According to the results of secondary electron cutoff (E_{cutoff}) and onset (E_{onset}) energies obtained in Figure 4f the optical band gap (E_g = 1.52 eV) calculated in combination with the ultraviolet absorption spectrum, the VBM of the sample are −5.25 and −5.21 eV respectively and the CBM are estimated to be −3.73 and −3.69 eV. The energy level arrangement diagram is in Figure 4g, the E_F and CBM of modified perovskite sample are improved. The enhanced E_F and CBM can effectively reduce the electron transport barrier and inhibit the recombination loss of interface non-radiation recombination, which can improve the carrier extraction capability of the corresponding D-PSK devices. The surface roughness and electric potential of the samples are characterized by atomic force microscopy (AFM). Figure 4h,j shows that the root mean square roughness of D-PSK is 26.75 nm, which is significantly reduced compared with 30.64 nm of N-PSK. This is consistent with the SEM results, indicating that the surface of the modified film is smoother, which is conducive to the spin-coating and high-quality growth of the ETL layer in devices. The Kelvin probe force microscopy (KPFM) measurement is performed in the same region characterized by AFM in Figure 4i,k, indicating that D-PSK has higher electronic chemical potential (ECP). Moreover, Figure S21 (Supporting Information) shows that D-PSK also has a more uniform potential, which contribute to better vertical carrier transport performance. All these characteristics illustrate that the D-PSK sample has better photoelectric performance than the traditional N-PSK, which will significantly improve the light absorption capacity and transport performance of the device.

The p–i–n planar PSCs with a configuration of ITO/MeO-2PACz/perovskite/PCBM/SnO_2/Ag are prepared to further study the effect of D-PSK samples on the photovoltaic performance of corresponding devices. The details of the specific fabrication process and parameters for device are demonstrated in SI. The cross-section SEM image shows the schematic diagram of the device structure, where MeO-2PACz/perovskite/PCBM are all prepared by spin-coating method and silver is prepared by vacuum coating (**Figure** 5a). Figure S22 (Supporting Information) shows the cross-section SEM image of N-PSK device prepared by solution method and Pb-based perovskite device. It apparently can be seen that the D-PSK device grown by doping method has fewer defects. It is worth mentioning that SnO_2 is prepared by ALD, which can effectively isolate the water and oxygen from the device. Figure S23 (Supporting Information) shows that perovskite covered by ALD-SnO_2 can still maintain the black phase in high humidity. Under standard lighting conditions (AM 1.5 G), the current–voltage (*J–V*) characteristics of the device are measured and the *PCE* of the device

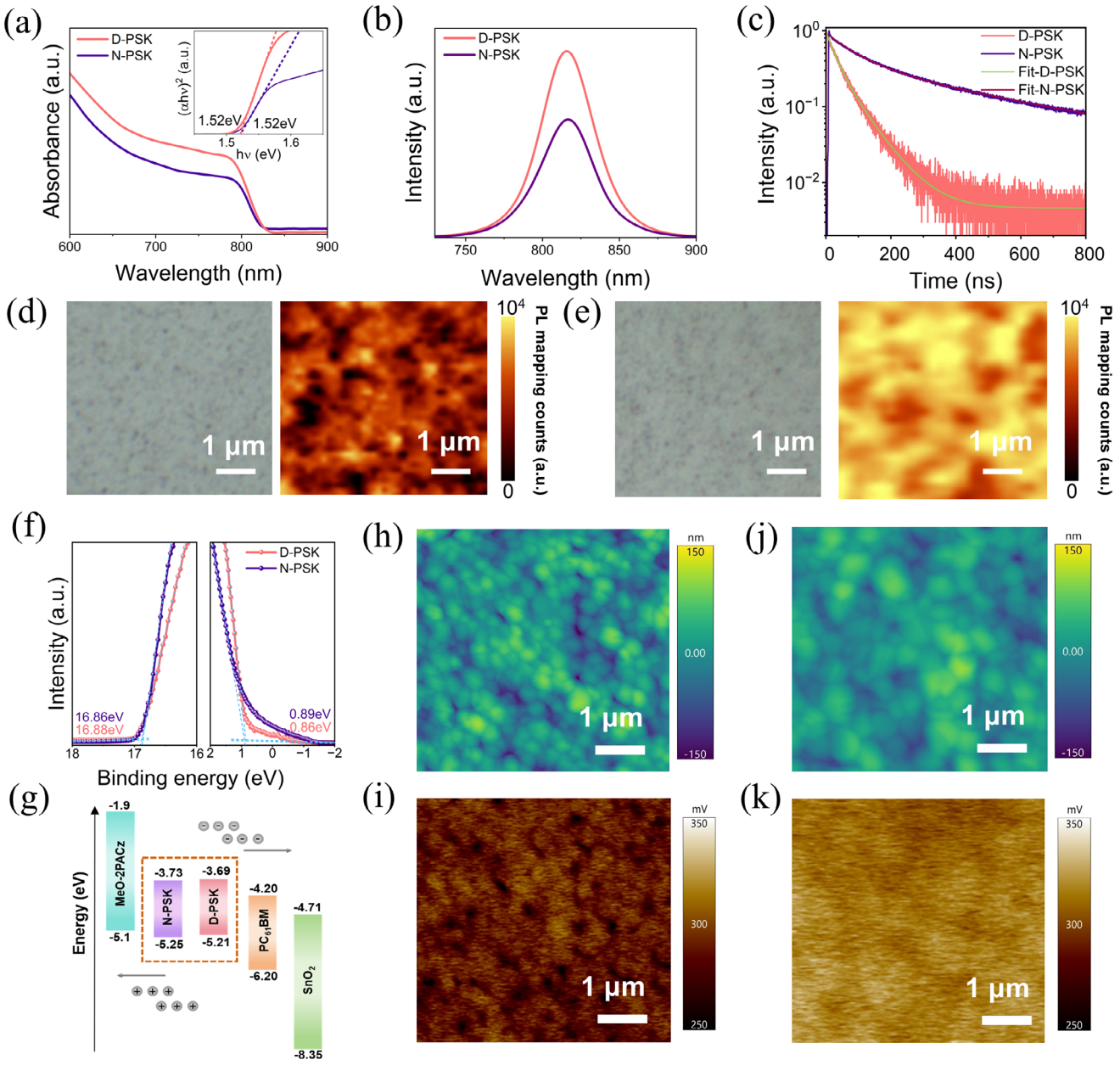

Figure 4. a) UV–vis absorption spectra and b) PL spectra of different films in normal Sn—Pb and doping Sn—Pb perovskite film. c) TRPL for half of devices made by N-PSK and D-PSK. d) Top-view confocal microscope and wide-field hyperspectral PL mapping images of d) N-PSK and e) D-PSK samples. Scale bars, 1 μm. f) UPS spectra of N/D-PSK samples. g) Energy-levels alignment of the device. The AFM images and surface potential of KPFM images of h,i) N-PSK and j,k) D-PSK samples.

corresponding to D-PSK increased from the initial 17.12% to 21.53% with N-PSK (Figure 5b). The N-PSK device has a V_{OC} of 0.91 V, J_{SC} of 25.69 mA cm^{-2} and fill factor (*FF*) of 73.21%, while the D-PSK devices has a V_{OC} of 1.00 V, J_{SC} of 26.87 mA cm^{-2} and *FF* of 80.13%. The significant enhancement of V_{OC}, J_{SC}, and *FF* can be attributed to fewer defects, lager grain size, better crystallinity, and superior photoelectric performance of D-PSK, which can be proven in previous experiments results.[46] In addition, the external quantum efficiency (EQE) of D-PSK device is also significantly higher than that of N-PSK device (Figure 5c), which can be attributed to the reduction of defects, more suitable energy level arrangement enhances carrier extraction and reduces non-radiative recombination illustrated in UPS measurements and energy-levels alignment. The results of the dark *J*–*V* curve show that under the condition of negative voltage reverse bias, the current of D-PSK device is lower than that of N-PSK device, indicating that the leakage current in PSCs is suppressed, which means that the defect density in the perovskite film is significantly decreased (Figure 5d). In the voltage range of 0.85–1.50 V the injection current density of D-PSK device is higher

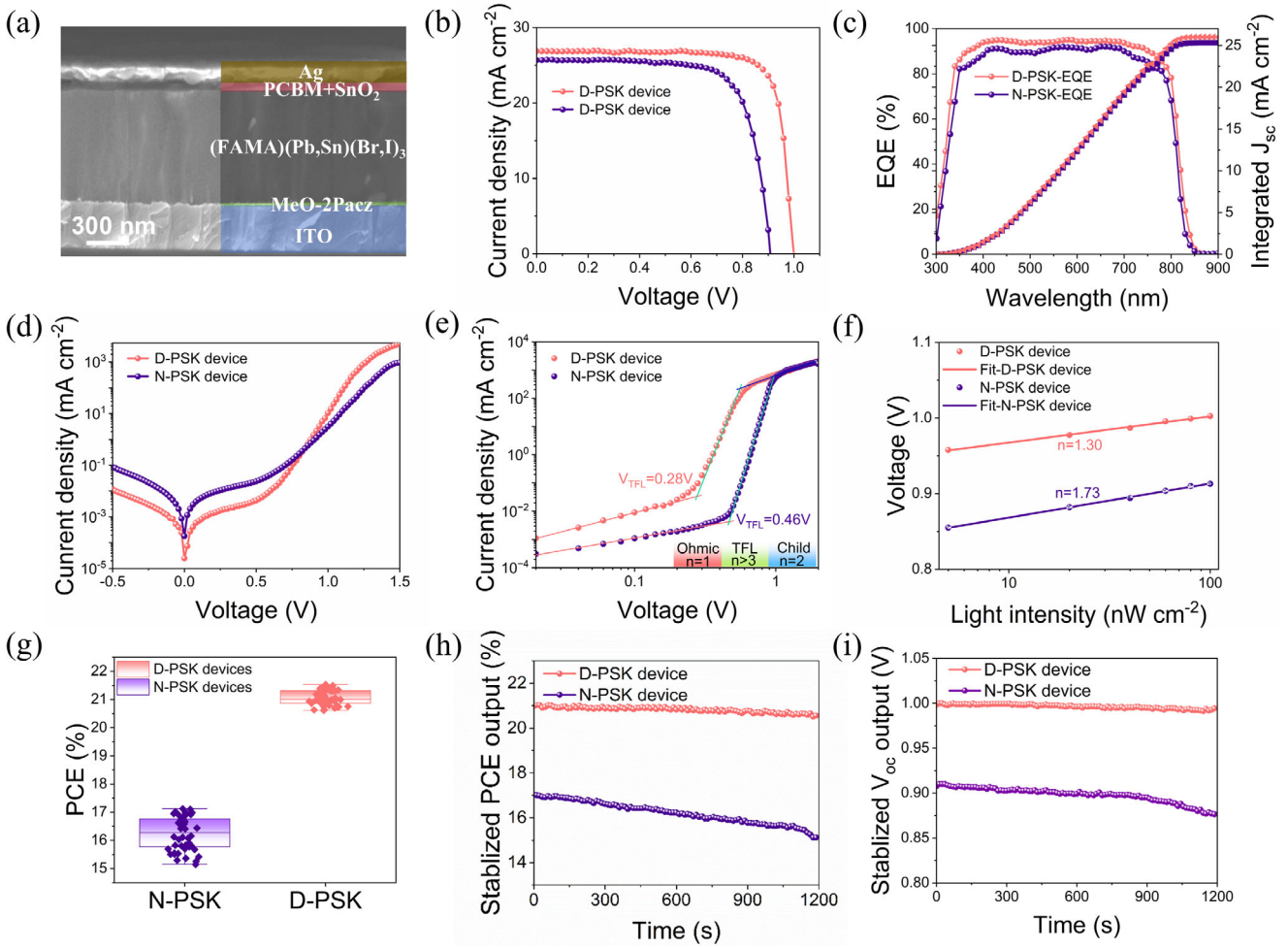

Figure 5. a) Cross-section SEM image of D-PSK PSCs. b) *J–V* measurements of N-PSK and D-PSK cells. c) EQE and integrated J_{SC} of the corresponding samples. d) Dark *J–V* measurements of PSCs and e) SCLC result of electron-only device. f) Dependence of V_{OC} on light intensity. g) Statistical distribution of *PCE*s of corresponding devices. h,i) V_{oc} and *PCE* measurement under continuous illumination.

than that of N-PSK device due to the improved carrier extraction and charge transfer ability of corresponding devices caused by more reasonable energy level arrangement in D-PSK. To further study the effect of D-PSK thin films on the defect state density of devices, the space charge-limited current (*SCLC*) method is applied to electron-only devices (ITO/SnO_2/perovskite/PCBM/Ag). Figure 5e shows that the trap filling limit voltage (V_{TFL}) corresponding of D-PSK is 0.28 V, while the V_{TFL} of N-PSK is 0.46 V. Using the formula $V_{TFL} = qN_tL^2/(2\varepsilon_r\varepsilon_0)$ (where q is the charge, N_t is the density of the trap state, L is the thickness of the perovskite film, ε_0 is the free space dielectric constant, ε_r is the relative dielectric constant of perovskite), the calculated electron trap state density of the N-PSK and D-PSK device is 6.51×10^{15} and 3.96×10^{15} cm^{-3}, respectively, which effectively further shows that fewer defects exist in the D-PSK film consistent to the previous SEM measurements.[50,51] To elucidate the carrier recombination dynamics in PSCs, we provided the relationship between V_{OC} and light intensity (Φ) (Figure 5f). The degree of trap-assisted shockley-reads-hall (SRH) recombination can be reflected by calculating the slope of the equation $\Delta V_{OC} = nk_BT\Delta\ln\Phi/q$ (k_B is the Boltzmann constant and T is the absolute temperature).[53,54] While the ideal factor n = 1, bimolecular recombination is dominant, for n = 2 trap-assisted SRH recombination dominates, the value of n is between 1 and 2.[54] The experimental results show that the slope of the N-PSK device is 1.77 k_BT/q after fitting, while the linear slope of the D-PSK battery is reduced to 1.30 k_BT/q, indicating that the SRH recombination assisted by the trap of the D-PSK device is significantly suppressed. The result is consistent with previous experimental results, which is related to the effective passivation of the perovskite thin films by HCOOH and the reduction of defects. Compared with traditional Sn—Pb hybrid perovskite devices, D-PSK thin films can effectively passivate defects in perovskite thin films, inhibit non-radiative recombination in PSCs, optimize the crystallinity of perovskite thin films and improve carrier extraction and charge transport performance resulting in high V_{OC}, high *FF* and J_{sc}. In addition, it can be seen that the champion efficiency of D-PSK devices is significantly higher than that of N-PSK devices (Figure 5g). In the statistic test of 50 devices, the *PCE* of D-PSK devices is generally higher than that of N-PSK devices and the voltage and current values of these devices are also shown, which indicates that D-PSK devices have general advantages of reproducible with higher PCE

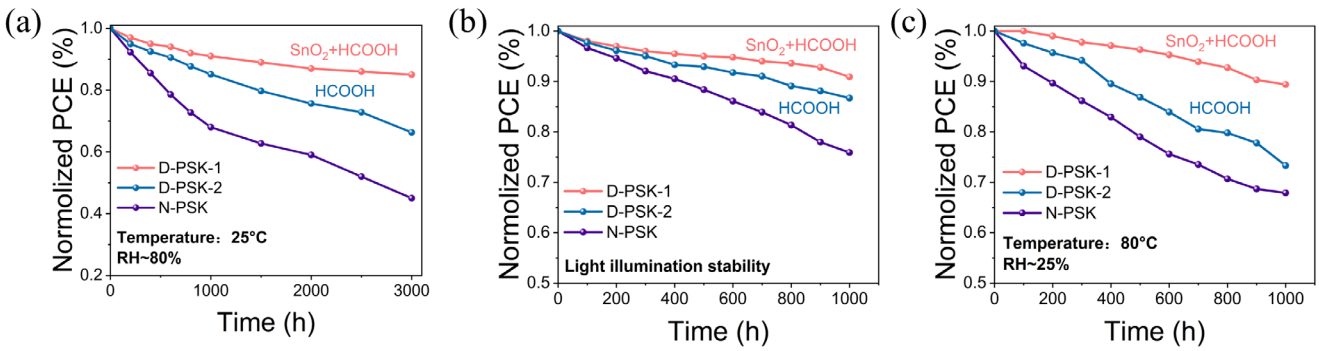

Figure 6. Long-term stability performance of three devices a) in ≈25 °C and ≈80% RH under air atmosphere and b) Light illumination in N_2 glovebox and c) thermal stability.

and smaller variance (Figure S24, Supporting Information). To confirm the energy output performance of the device, we test the time-dependent PCEs of the PSCs at 12 s intervals under continuous AM 1.5 G illumination (Figure 5h,i). During the stability test with a total time length of 20 min every 12 s interval, the *PCE* and V_{oc} output stability of D-PSK device is obviously better than that of N-PSK device, which can be attributed to fewer defect and higher stability of D-PSK device.

The serious issue of Sn—Pb hybrid PSCs is poor stability. Three different type devices (a. D-PSK-1 device: ITO/MeO-2PACz/D-PSK/PCBM/SnO_2/Ag; b. D-PSK-2 device:ITO/MeO-2PACz/D-PSK/PCBM/Ag; c. N-PSK device: ITO/MeO-2PACz/N-PSK/PCBM/Ag;) were constructed to verify the effects of HCOOH and ALD-SnO_2 respectively. The device performance affected by ALD parameter is shown in Figure S25 and Table S1 (Supporting Information). Champion devices were obtained with condition (TDMASn dose: H_2O dose = 100 ms: 20 ms, 80 cycles). In order to more fully evaluate the stability, different extreme condition tests were applied on the devices.[55] **Figure 6a** shows the storage of an unencapsulated D-PSK-1 device in an air atmosphere for 3000 h (temperature: ≈25 °C, relative humidity (RH)): ≈80%) can still maintain more than 85% of the initial normalized *PCE* (21.53%), whereas the *PCE* of an unsealed N-PSK device can only retain 45% of the initial *PCE* (17.12%). D-PSK-2 device can maintain 66%, it can contribute to the reducing and passivating effect of HCOOH. Figure 6b illustrates that D-PSK-1 device could maintain 91% under continuous 1 sun illumination conditions in the N_2 glovebox, while the D-PSK-2 and N-PSK device would decay to 86% and 76% of initial *PCE*. The same trend is also shown in the test of thermal stability in Figure 6c. The *PCE* of D-PSK-2 device would decay faster in the thermal test than two former tests, which could be attributed to the decomposition of HCOOH at high temperature. These results indicate that HCOOH would play the role of passivation and reduction effect, ALD-SnO_2 effectively could diminish water and oxygen damage and effectively prevents the decomposition of formic acid.[56] Moreover, Figure S26 (Supporting Information) shows the changes of N-PSK and D-PSK film samples after aging in the air atmosphere, which shows that N-PSK is decomposed while D-PSK film still maintains the basic black phase. To further verify significant improvement of hydrophobic characteristics in D-PSK device, the water contact angle of different samples is tested in Figure S27 (Supporting Information). It can be seen that the contact angle of N-PSK and D-PSK film are 66 and 86°, which indicates D-PSK film exhibits more excellent hydrophobic performance than N-PSK. This can be attributed to the optimized crystal quality of the perovskite film by HCOOH, improving the hydrophobicity of perovskite film.[57,58]

3. Conclusion

In summary, we report a novel gradient doping strategy to prepare stable Sn—Pb mixed perovskite with high crystalline quality by replacing Pb^{2+} in perovskite with Sn^{2+} and doping under HCOOH coordination. In this strategy, the infiltration of $HCOO^-$ can effectively inhibit the degradation of perovskite due to oxidation and deprotonation reaction. The interaction with Sn^{2+} and Pb^{2+} can effectively reduce the vacancy defects in perovskite and improve the stability of the device. The dense SnO_2 prepared by ALD further improves the device stability. Through doping and passivation modification of the material, the charge transfer capability of the device is improved due to more suitable band gap and energy level alignment. Eventually, the champion device we prepared achieved a *PCE* of 21.53% and V_{oc} of 1.00 V with significantly improved stability in long-term stability tests. This method provides a novel idea for synthesis of Sn—Pb perovskite and effectively solves the problem of uncontrollable crystallization of Sn—Pb perovskite. On the basis of this strategy, further optimization of the underlying Pb-based perovskite can provide the possibility for further breakthroughs in the efficiency of Sn—Pb hybrid PSCs.

Supporting Information

Supporting Information is available from the Wiley Online Library or from the author.

Acknowledgements

This work was supported by the Natural Science Foundation of China (11834011) and the Shanghai New Energy Technology Research and Development Project of 24DZ3000900.

Conflict of Interest

The authors declare no conflict of interest.

Data Availability Statement

The data that support the findings of this study are available from the corresponding author upon reasonable request.

Keywords

deprotonation reaction, doping growth method, energy level alignment, grain size, defect passivation, reductive Sn^{2+}, Sn—Pb mixed perovskite solar cells

Received: January 10, 2025
Revised: March 13, 2025
Published online: March 26, 2025

[1] J. R. Poindexter, R. L. Z. Hoye, L. Nienhaus, R. C. Kurchin, A. E. Morishige, E. E. Looney, A. Osherov, J. P. Correa-Baena, B. Lai, V. Bulovic, V. Stevanovic, M. G. Bawendi, T. Buonassisi, *ACS Nano.* **2017**, *11*, 7101.
[2] Z. Saki, M. M. Byranvand, N. Taghavinia, M. Kedia, M. Saliba, *Energy Environ. Sci.* **2021**, *14*, 5690.
[3] F. Hao, C. C. Stoumpos, R. P. H. Chang, M. G. Kanatzidis, *J. Am. Chem. Soc.* **2014**, *136*, 8094.
[4] H. Liu, Z. Zhang, W. Zuo, R. Roy, M. Li, M. M. Byranvand, M. Saliba, *Adv. Energy Mater.* **2023**, *13*, 32.
[5] J. H. Noh, S. H. Im, J. H. Heo, T. N. Mandal, S. I. Seok, *Nano Lett.* **2013**, *13*, 1764.
[6] Q. Jiang, J. Tong, Y. Xian, R. A. Kerner, S. P. Dunfield, C. Xiao, R. A. Scheidt, D. Kuciauskas, X. Wang, M. P. Hautzinger, *Nature* **2022**, *611*, 278.
[7] C. Li, Z. Song, C. Chen, C. Xiao, B. Subedi, S. P. Harvey, N. Shrestha, K. K. Subedi, L. Chen, D. Liu, Y. Li, Y. W. Kim, C. Jiang, M. J. Heben, D. Zhao, R. J. Ellingson, N. J. Podraza, M. Al-Jassim, Y. F. Yan, *Nat. Energy* **2020**, *5*, 768.
[8] R. Lin, J. Xu, M. Wei, Y. Wang, Z. Qin, Z. Liu, J. Wu, K. Xiao, B. Chen, S. M. Park, *Nature* **2022**, *603*, 73.
[9] A. Kojima, K. Teshima, Y. Shirai, T. Miyasaka, *J. Am. Chem. Soc.* **2009**, *131*, 6050.
[10] M. M. Lee, J. Teuscher, T. Miyasaka, T. N. Murakami, H. J. Snaith, *Science* **2012**, *338*, 643.
[11] Y. Zhao, F. Ma, Z. H. Qu, S. Q. Yu, T. Shen, H. X. Deng, X. B. Chu, X. X. Peng, Y. B. Yuan, X. W. Zhang, J. B. You, *Science* **2022**, *377*, 531.
[12] W. Ke, M. G. Kanatzidis, *Nat. Commun.* **2019**, *10*, 965.
[13] C. Liu, J. Tu, X. T. Hu, Z. Q. Huang, X. C. Meng, J. Yang, X. P. Duan, L. C. Tan, Z. Li, Y. W. Chen, *Adv. Funct. Mater.* **2019**, *29*, 9.
[14] W. Yang, F. Igbari, Y. Lou, Z. u. Wang, L. h. Liao, *Adv. Energy Mater.* **2019**, *10*, 1902584.
[15] L. Mao, C. C. Stoumpos, M. G. Kanatzidis, *J. Am. Chem. Soc.* **2019**, *141*, 1171.
[16] H. Tsai, W. Nie, J.-C. Blancon, C. C. Stoumpos, R. Asadpour, B. Harutyunyan, A. J. Neukirch, R. Verduzco, J. J. Crochet, S. Tretiak, L. Pedesseau, J. Even, M. A. Alam, G. Gupta, J. Lou, P. M. Ajayan, M. J. Bedzyk, M. G. Kanatzidis, A. D. Mohite, *Nature* **2016**, *536*, 312.
[17] Z. Liu, H. Yang, J. Wang, Y. Yuan, K. Hills-Kimball, T. Cai, P. Wang, A. Tang, O. Chen, *Nano Lett.* **2021**, *21*, 1620.
[18] F. Lin, H. Wang, H. Lin, W. Liu, J. Li, *Chem. Commun.* **2021**, *57*, 1754.
[19] E. Jokar, C. H. Chien, C. M. Tsai, A. Fathi, E. W. G. Diau, *Adv. Mater.* **2019**, *31*, 1804835.
[20] I. Kopacic, B. Friesenbichler, S. F. Hoefler, B. Kunert, H. Plank, T. Rath, G. Trimmel, *ACS Appl. Energy Mater.* **2018**, *1*, 343.
[21] M. H. Kumar, S. Dharani, W. L. Leong, P. P. Boix, R. R. Prabhakar, T. Baikie, C. Shi, H. Ding, R. Ramesh, M. Asta, *Adv. Mater.* **2014**, *26*, 7122.
[22] M. Konstantakou, T. Stergiopoulos, *J. Mater. Chem. A* **2017**, *5*, 11518.
[23] H. Li, W. Zhang, *Chem. Rev.* **2020**, *120*, 9835.
[24] W. Shockley, H. J. Queisser, *J. Appl. Phys.* **1961**, *32*, 510.
[25] P. C. Zhu, J. Zhu, *Nat. Energy* **2022**, *7*, 570.
[26] G. E. Eperon, T. Leijtens, K. A. Bush, R. Prasanna, T. Green, J. Wang, D. P. McMeekin, G. Volonakis, R. L. Milot, R. May, A. Palmstrom, D. J. Slotcavage, R. A. Belisle, J. B. Patel, E. S. Parrott, R. J. Sutton, W. Ma, F. Moghadam, B. Conings, A. Babayigit, H. G. Boyen, S. Bent, F. Giustino, L. M. Herz, M. B. Johnston, M. D. McGehee, H. J. Snaith, *Science* **2016**, *354*, 861.
[27] J. Tong, Z. Song, D. H. Kim, X. Chen, C. Chen, A. F. Palmstrom, P. F. Ndione, M. O. Reese, S. P. Dunfield, O. G. Reid, J. Liu, F. Zhang, S. P. Harvey, Z. Li, S. T. Christensen, G. Teeter, D. Zhao, M. M. Al-Jassim, M. van Hest, M. C. Beard, S. E. Shaheen, J. J. Berry, Y. Yan, K. Zhu, *Science* **2019**, *364*, 475.
[28] S. Zhou, S. Q. Fu, C. Wang, W. W. Meng, J. Zhou, Y. R. Zou, Q. X. Lin, L. S. Huang, W. J. Zhang, G. J. Zeng, D. X. Pu, H. L. Guan, C. Wang, K. L. Dong, H. S. Cui, S. X. Wang, T. Wang, G. J. Fang, W. J. Ke, *Nature* **2023**, *624*, 69.
[29] B. Li, H. Di, B. Chang, R. Yin, L. Fu, Y. Zhang, L. Yin, *Adv. Funct. Mater.* **2021**, *31*, 9.
[30] D. Meggiolaro, D. Ricciarelli, A. A. Alasmari, F. A. S. Alasmary, F. De Angelis, *J. Phys. Chem. Lett.* **2020**, *11*, 3546.
[31] B. Yu, Z. Chen, Y. Zhu, Y. Wang, B. Han, G. Chen, X. Zhang, Z. Du, Z. He, *Adv. Mater.* **2021**, *33*, 10.
[32] X. Meng, T. Wu, X. Liu, X. He, T. Noda, Y. Wang, H. Segawa, L. Han, *J. Phys. Chem. Lett.* **2020**, *11*, 2965.
[33] Y. Liao, H. Liu, W. Zhou, D. Yang, Y. Shang, Z. Shi, B. Li, X. Jiang, L. Zhang, L. Quan, *J. Am. Chem. Soc.* **2017**, *139*, 6693.
[34] X. Meng, J. Lin, X. Liu, X. He, L. Han, *Adv. Mater.* **2019**, *31*, 1903721.
[35] J. Cao, L. Hok-Leung, Y. Xu, X. Guo, N. Wang, C.-k. Liu, T. Wang, H. Cheng, Y. Zhu, M. G. Li, W. Wai-Yeung, F. Yan, *Adv. Mater.* **2022**, *34*, 2107729.
[36] R. Lin, K. Xiao, Z. Qin, Q. Han, C. Zhang, M. Wei, M. I. Saidaminov, Y. Gao, J. Xu, M. Xiao, A. Li, J. Zhu, E. H. Sargent, H. Tan, *Nat. Energy* **2019**, *4*, 864.
[37] Q. Chen, J. Luo, R. He, H. Lai, S. Ren, Y. Jiang, Z. Wan, W. Wang, X. Hao, Y. Wang, J. Zhang, I. Constantinou, C. Wang, L. Wu, F. Fu, D. Zhao, *Adv. Energy Mater.* **2021**, *11*, 2101045.
[38] T. Shi, H.-S. Zhang, W. Meng, Q. Teng, M. Liu, X. Yang, Y. Yan, H.-L. Yip, Y.-J. Zhao, *J. Mater. Chem. A* **2017**, *5*, 15124.
[39] A. Muhammad, T. Chowdhury, K. Matsuishi, I. Bedja, Y. Moritomo, A. Islam, *Sol. RRL* **2021**, *5*, 2000606.
[40] Y. Su, J. Yang, G. Liu, W. Sheng, J. Zhang, Y. Zhong, L. Tan, Y. Chen, *Adv. Funct. Mater.* **2022**, *32*, 2109631.
[41] E. Jokar, H. Chuang, C. Kuan, H. Wu, C. Hou, J. Shyue, W. G. Diau, *J. Phys. Chem. Lett.* **2021**, *12*, 10106.
[42] K. P. Marshall, M. Walker, R. I. Walton, R. A. Hatton, *Nat. Energy.* **2016**, *1*, 16178.
[43] T. B. Song, T. Yokoyama, C. C. Stoumpos, J. Logsdon, D. Cao, M. R. Wasielewski, S. Aramaki, M. G. Kanatzidis, *J. Am. Chem. Soc.* **2017**, *139*, 836.
[44] J. Jeong, M. Kim, J. Seo, H. Lu, P. Ahlawat, A. Mishra, Y. Yang, M. A. Hope, F. T. Eickemeyer, M. Kim, Y. J. Yoon, I. W. Choi, B. P. Darwich, S. J. Choi, Y. Jo, J. H. Lee, B. Walker, S. M. Zakeeruddin, L. Emsley, U. Rothlisberger, A. Hagfeldt, D. S. Kim, M. Graetzel, J. Y. Kim, *Nature* **2021**, *592*, 381.
[45] Y. Liu, Y. Zhang, X. Zhu, Z. Yang, S. F. Liu, *Sci. Adv.* **2021**, *7*, abc8844.
[46] C. Gao, H. Zhang, F. Qiao, H. Huang, D. Zhang, D. Ding, D. Du, J. Liang, J. Bao, H. Liu, W. Shen, *Nano Energy* **2023**, *116*, 108765.

[47] X. Jiang, Z. Zang, Y. Zhou, H. Li, Z. Ning, *Acc. Mater. Res.* **2021**, *2*, 210.
[48] S. Du, H. Huang, Z. Lan, P. Cui, L. Li, M. Wang, S. Qu, L. Yan, C. Sun, Y. Yang, X. Wang, M. Li, *Nat. Commun.* **2024**, *15*, 5223.
[49] Q. Wang, J. Xiong, Y. Xing, X. Gan, W. Zhu, R. Xuan, X. Liu, L. Huang, Y. Zhu, J. Zhang, *Adv. Sci.* **2024**, *11*, 2400962.
[50] H. Ren, S. Yu, L. Chao, Y. Xia, Y. Sun, S. Zuo, F. Li, T. Niu, Y. Yang, H. Ju, B. Li, H. Du, X. Gao, J. Zhang, J. Wang, L. Zhang, Y. Chen, W. Huang, *Nat. Photonics* **2020**, *14*, 154.
[51] S. Xiong, Z. Hou, S. Zou, X. Lu, J. Yang, T. Hao, Z. Zhou, J. Xu, Y. Zeng, W. Xiao, W. Dong, D. Li, X. Wang, Z. Hu, L. Sun, Y. Wu, X. Liu, L. Ding, Z. Sun, M. Fahlman, Q. Bao, *Joule* **2021**, *5*, 467.
[52] T. He, S. Li, Y. Jiang, C. Qin, M. Cui, L. Qiao, H. Xu, J. Yang, R. Long, H. Wang, M. Yuan, *Nat. Commun.* **2020**, *11*, 11.
[53] Q. Jiang, Y. Zhao, X. Zhang, X. Yang, Y. Chen, Z. Chu, Q. Ye, X. Li, Z. Yin, J. You, *Nat. Photonics* **2019**, *13*, 460.
[54] G. Wetzelaer, M. Scheepers, A. M. Sempere, C. Momblona, J. Avila, H. J. Bolink, *Adv. Mater.* **2015**, *27*, 1837.
[55] S. Qu, H. Huang, J. Wang, P. Cui, Y. Li, M. Wang, L. Li, F. Yang, C. Sun, Q. Zhang, P. Zhu, Y. Wang, M. Li, *Angew. Chem., Int. Ed.* **2024**, *137*, 202415949.
[56] D. Gao, B. Li, Q. Liu, C. Zhang, Z. Yu, S. Li, J. Gong, L. Qian, F. Vanin, K. Schutt, M. A. Davis, A. F. Palmstrom, S. P. Harvey, N. J. Long, J. M. Luther, X. Zeng, Z. Zhu, *Science* **2024**, *386*, 187.
[57] L. He, H. Zhang, D. Zhang, C. Gao, H. Su, D. Du, D. Ding, H. Liu, W. Shen, *Adv. Funct. Mater.* **2024**, *34*, 2403020.
[58] L. He, H. Su, Z. Li, H. Liu, W. Shen, *Adv. Funct. Mater.* **2023**, *33*, 2213963.